

## SOLAR MICROWAVE BURSTS AND INJECTION PITCH-ANGLE DISTRIBUTION OF FLARE ELECTRONS

J. LEE AND DALE E. GARY

Physics Department, New Jersey Institute of Technology, 323 M. L. King Boulevard, Newark, NJ 07102

Received 1999 November 10; accepted 2000 June 19

### ABSTRACT

We calculate the time variation of the energy and pitch angle of high-energy electrons injected into a magnetic loop and subsequently trapped there because of magnetic mirroring. We use the evolving distribution in the calculation of gyrosynchrotron emission, as an aid to interpretation of a particular microwave burst observed using the Owens Valley Solar Array (OVSA) during a GOES class C2.8 flare on 1993 June 3. The electrons are assumed to have a Gaussian pitch-angle distribution, whose width and mean pitch angle are calculated as they evolve in time, taking into account the electron energy loss and a specific magnetic loop structure set as a model for the target active region. Various temporal behaviors of the microwave spectrum are found as a function of injection and trap conditions, which can be used to infer some of the injection properties directly from the observed microwave spectra. As a main result we found that initial pitch-angle distribution plays an important role in the microwave spectral evolution. This is largely due to the fact that pitch-angle diffusion of electrons under Coulomb collisions markedly differs at those electron energies to which the microwave spectrum is sensitive. This effect cannot be reproduced by adjusting the trap properties and therefore could be used to determine whether the initial pitch-angle distribution is isotropic or narrowly beamed. The microwave burst spectra observed during the 1993 June 3 flare are found to be most consistent with the hypothesis of an initially narrow beamed injection ( $\leq 30^\circ$ ) into a low-density ( $\sim 4 \times 10^9 \text{ cm}^{-3}$ ) magnetic trap. This result explains the observed asymmetric microwave time curve consisting of a relatively short rise ( $\sim 32 \text{ s}$ ) and a long decay ( $\geq 5 \text{ minutes}$ ) in terms of a transport effect rather than acceleration characteristics. The physical connection of the proposed microwave model to hard X-ray models in thin/thick targets is briefly discussed.

*Subject headings:* Sun: flares — Sun: magnetic fields — Sun: radio radiation

### 1. INTRODUCTION

The high-energy neutral radiations such as hard X-rays, gamma rays, and microwaves carry information about physical properties of particles accelerated during solar flares. In deriving the information, all of the observed time, spatial, and spectral properties will be important. Of particular importance for understanding the physical mechanism of electron acceleration will be the spectral morphology as it reflects the electron distribution in energy and pitch angle. When one infers information about electron acceleration from observed radiation spectra, it is, however, necessary to deal with several transport effects that modify the electron distribution in phase space as determined by the acceleration mechanism (see, e.g., Petrosian, McTiernan, & Marschhauser 1994). In this regard, the topic of trapping of flare-produced electrons in magnetic loops and their evolution under Coulomb collisions has received considerable attention because these are the processes expected to always be present and have great influence on the life of electrons accelerated during solar flares.

A huge number of both observational and theoretical papers have been published on the topic of Coulomb collisions and magnetic trapping (see Aschwanden et al. 1997, and references therein). For our purpose we only briefly review some of the main scientific outputs that these studies have yielded. First, in the earliest trap model, Takakura & Kai (1966) modeled high-energy electrons evolving under Coulomb collisions and synchrotron loss in a uniform, perfect trap model. Melrose & Brown (1976) developed a trap-and-precipitation model, which accommodates both trapped and precipitating populations of electrons in order

to handle both hard X-ray thick target and thin target models in one context. Both papers look for spectral characteristics as evidence for the effect of Coulomb collisions on electrons, which can then be used to derive acceleration properties through spectral analysis of the resulting radiations. Recently Aschwanden (1998) has incorporated the trap and precipitation process into inversion of the observed hard X-ray spectrum to obtain the injection spectrum. Second, Bai & Ramaty (1979) found, in a more generalized treatment of the Coulomb collisions in the presence of magnetic fields, that energy-dependent delay of electrons will necessarily occur under Coulomb collisions when the electron injection continues over a finite time. The amount of time delay is a function of ambient density in the trap (hereafter, trap density) and could be used to determine the trap density (Vilmer, Kane, & Trotter 1982; Bruggmann et al. 1994). For some events, the density required for explaining the time delay under Coulomb collisions is too low compared with that needed to explain the observed hard X-ray flux, and it leads to a hypothesis that high-energy acceleration should actually occur in a temporally separate stage (Bai & Ramaty 1979). The time delay as a density diagnostic has recently been applied to a large number of samples from *Compton Gamma Ray Observatory* (CGRO)/BATSE (Aschwanden et al. 1997). Third, as theoretical models developed it became possible to predict the electron energy and pitch-angle distribution within inhomogeneous magnetic loops in the presence of Coulomb and other effects (Leach & Petrosian 1981; Bai 1982; Lu & Petrosian 1988; Miller & Ramaty 1989; McTiernan & Petrosian 1990; Zharkova, Brown, & Syriavskii 1995). These models

can predict the pitch-angle distribution of electrons (as well as their energy distribution) as a function of time and space and, thus, polarization of resulting hard X-ray emissions. Comparison of such models with hard X-ray observations can lead to information on the injection (beam) properties as well as the trap properties (McTiernan & Petrosian 1990; Zharkova et al. 1995). Fourth, Fletcher (1996) has carried out numerical simulation of stochastic diffusion of nonrelativistic electrons within inhomogeneous magnetic loop models, which explains the location of hard X-ray sources above the soft X-ray loop. It is also noteworthy that a recent time of flight study performed by Aschwanden et al. (1996) placed the acceleration site well above the radiating loop where trap and precipitation occur, so that the electron properties at the time of entering the loop (to which we refer as “injection”) may not be exactly the same as those at acceleration. It is also known that Coulomb collisions within the acceleration site have an influence on the electron distribution different from that during transport (Petrosian et al. 1994). Thus, they need to be distinguished from each other. Fifth, the energy dependence of Coulomb collisional loss has also been used to explain the apparent discrepancy between the electrons emitting hard X-rays and microwaves, respectively, in terms of total number of radiating electrons, injection function (seed particles), and time delays between hard X-ray and microwave maxima (Klein, Trotter, & Magun 1986; Bruggmann et al. 1994; Mel’nikov 1994). It also gives an explanation of the commonly observed spectral hardening (flattening) during decay in terms of electron evolution under Coulomb collisions, as an alternative to a more conventional idea that spectral hardening in the decay is actually that of the acceleration spectrum (Mel’nikov 1994). From these works we may draw a general conclusion as follows: an observed radiation spectrum would represent a combination of acceleration and the transport effect, which cannot, in general, be separated. However, in the case where the transport process is dominated by Coulomb collisions, we may possibly separate one from the other, as the involved physics is well known. Fortunately, there are some observational signatures by which we can identify the dominance of Coulomb collisional effect on the electrons, and we can use them to determine the acceleration and trap conditions.

In this paper we use the knowledge obtained from these studies for a physical interpretation of microwave spectral observations. The microwave spectrum in the optically thin range is a direct measure of the electron energy distribution and can be used as a tool for exploring electron evolution in phase space (Petrosian 1981; Dulk & Marsh 1982). In order to do that we first have to make sure that the event is indeed dominated by Coulomb collisions. As will be discussed in the next section, we choose an event that we identify as dominated by Coulomb collisions from the observed spectral flattening and radio morphology in comparison with magnetic fields. As a matter of fact, there appears to be a significant percentage of such events that show spectral flattening in the decay phase, in burst spectra obtained with the Owens Valley Solar Array (OVSA; Silva, Wang, & Gary 2000). In order to predict the evolution of electrons in phase space and the resulting radiation given the trapping environment, we need a set of theoretical tools and a basic framework on which to build such a model. It can immediately be noticed that a simplified model with isotropic pitch-angle distribution in a homogeneous source with no

magnetic structure specified (Takakura & Kai 1966; Melrose & Brown 1976; Vilmer et al. 1982; Mel’nikov 1994) is inappropriate to handle our case. More appropriate to handle a weak pitch-angle diffusion case are models in which electron pitch angle may change in association with the magnetic field variation (Leach & Petrosian 1981; Bai 1982; Lu & Petrosian 1988; Miller & Ramaty 1989; McTiernan & Petrosian 1990; Zharkova et al. 1995).

Although most desirably the whole picture should be considered including acceleration, injection, and interaction of precipitating electrons with the lower atmosphere, we limit our investigation in this paper to the extent of electron injection and magnetic trapping. Namely, we assume that the electrons radiating microwaves begin their lives in a magnetic trap with initial conditions specified by the injection function and evolve in phase space under Coulomb collisions within the trap. This picture is based on the generally accepted notion that microwaves are mostly due to electrons trapped in the coronal part of the loop. The transport effect here refers to the effects of Coulomb collisions accumulating along the total path of electrons during multiple bounces within the magnetic trap. The transport effect during one transit time itself is ignored (in contrast to the time of flight study by Aschwanden et al. 1996), for we are dealing with lifetimes under Coulomb collisions that are much longer than one transit time, in agreement with the observations, discussed in § 2, that motivate this work. This simplification allows us to use analytical Fokker-Planck solutions known for each case and allows a means to parameterize the problem in a simple form. We include electron escape from the trap as a loss mechanism but also briefly discuss interaction of those electrons with the lower atmosphere, only to determine the proportion of thin to thick target hard X-ray emissions.

The plan of this paper is as follows: a brief description of the observation that motivates this work is given in § 2 together with qualitative interpretation. We present the formulation to be used in § 3, describe the model predictions in § 4, and then apply the model to the microwave observation in § 5. We briefly discuss the hard X-ray counterpart in § 6 and conclude in § 7.

## 2. OBSERVATION

The motivating observation is that of a microwave burst that occurred on 1993 June 3 (23:22 UT) during a C2.8 flare in *GOES* SX class made using the OVSA. The temporal behavior of microwave flux is highly asymmetric (like that of other microwave bursts); at 7 GHz range, the event peaked in less than 1 minute and decayed over longer than 5 minutes, during which the microwave spectrum shows progressive flattening at high frequencies. Details of the observations are presented in a companion paper (Lee et al. 2000). Here we briefly discuss why we consider the observed spectral variation to be mainly due to Coulomb collisions but not mainly due to an acceleration effect.

The upper panel of Figure 1 shows the radio morphology of the event. The observations show a single source at a low frequency (5 GHz) and double sources at high frequencies (11–17 GHz). A soft X-ray loop from *Yohkoh*/SXT is seen to connect these radio sources at different frequencies. Because of the dependence of microwave emission on magnetic field strength, these two sources could be interpreted, respectively, as an optically thick source at the loop top and thin sources at the footpoints of a single loop (cf. Kundu, White,

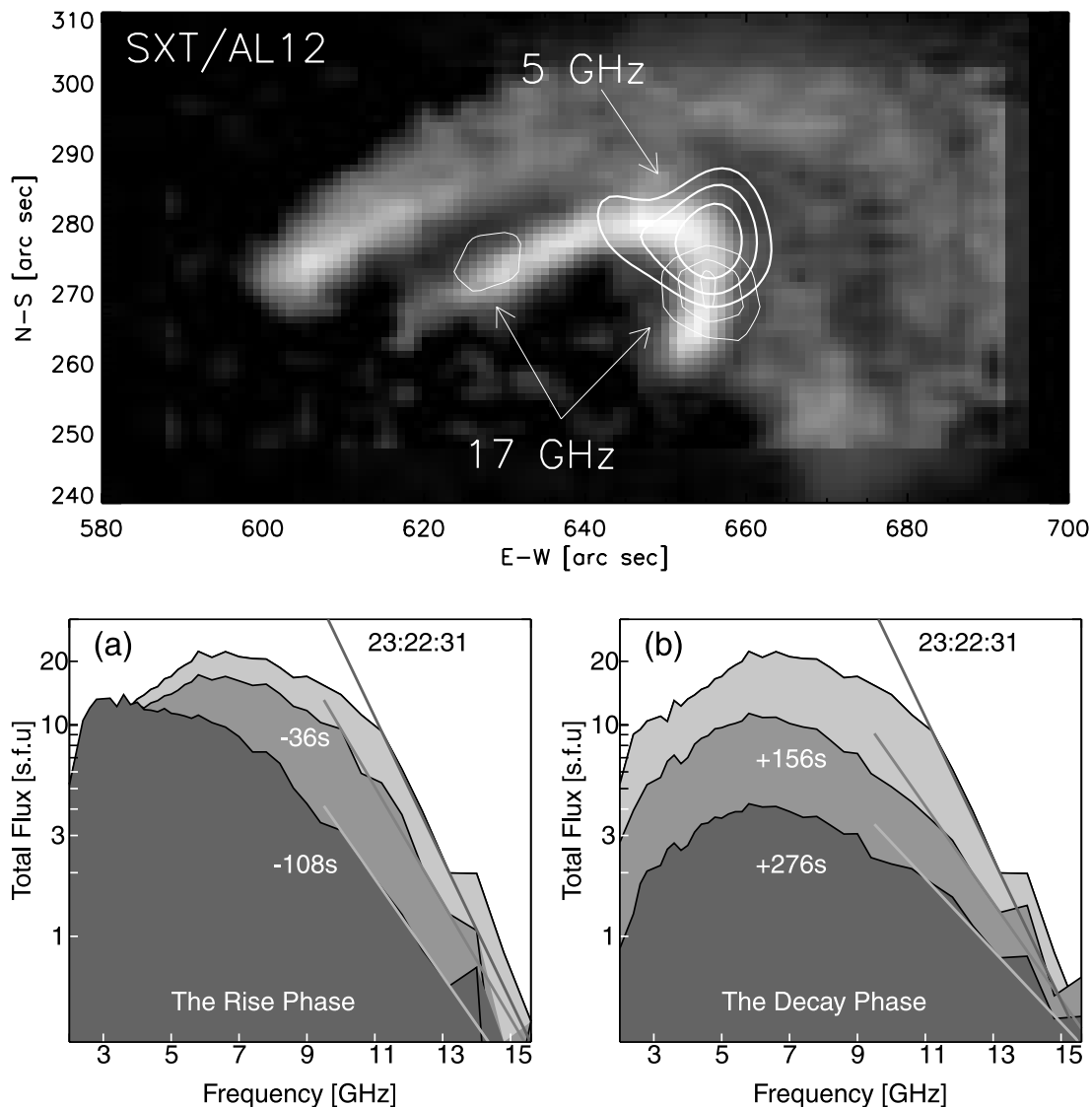


FIG. 1.—Microwave data obtained during the 1993 June 3 flare. *Top*: Radio intensity peaks (*contours*) on top of a soft X-ray image from a filtered *Yohkoh* SXT/AL12 at 23:29 UT. Contours are 80% to 99% of the maximum intensities:  $1.8 \times 10^7$  K at 5 GHz and  $1.2 \times 10^5$  K at 17 GHz, respectively. *Bottom*: Spectral variation in the microwave total power during (a) the rise and (b) the decay phases, at five selected times relative to the time of the maximum flux (23:22:31 UT). The straight lines are guide lines for spectral slope at the corresponding times.

& Schmahl 1989; Nindos et al. 2000). We then regard it as significant that the western component of the double peaks does not reach the footpoint whereas the eastern component does (Lee et al. 2000). A vector magnetogram obtained at Mees Solar Observatory (courtesy of A. Pevtsov) shows an asymmetry in field strength at the two ends of the loop. We therefore conclude that the morphology indicates an actual vacancy of high-energy electrons in the unseen part of the loop. Our explanation is that the injected electrons with low pitch angles, smaller than the loss cone angle, precipitate immediately into the chromosphere on the eastern side of the loop (cf. Melrose & White 1979). Only those with pitch angles higher than that can survive and bounce back toward the west where they reach a magnetic mirroring point that lies well above the western footpoint. This scenario seems plausible in view of the large magnetic flux imbalance observed between the two footpoints on the magnetogram but requires that the electron

pitch-angle scattering should be “weak” as in the original definition by Kennel (1969).

The lower panels in Figure 1 show the variation of the total power spectrum during the event. As shown here, the spectral slope on the high-frequency side changes in a hard-soft-hard pattern, but after subtracting the spectrum of a previous burst that occurred just before this event, the spectral slope is more or less constant in the rise phase and in the decay phase it hardens with time (see Lee et al. 2000). This spectral hardening is most simply interpreted as due to the influence of Coulomb collisions on trapped electrons that were injected with a constant energy distribution (Mel’nikov 1994; Mel’nikov & Magun 1998). Furthermore, this hypothesis of Coulomb collision in combination with a low ambient density can also lead to a weak pitch-angle diffusion as needed to explain the observed morphology (cf. Melrose & White 1979). On this basis, we proceed to analyze this particular type of microwave spectral evolution

in terms of a model for electrons trapped in converging magnetic fields undergoing Coulomb collisions.

As an aside, we note that it is also possible that the observed spectral variation could be due to a continued acceleration in just such a way as to mimic the observed microwave spectrum without any propagation effect. However, interpreting the radiation as mainly controlled by an acceleration process, we require a very efficient energy loss mechanism with a timescale much shorter than that of acceleration. Major energy loss mechanisms for electrons during solar flares are Coulomb collisions and precipitation into the chromosphere (e.g., Melrose & Brown 1976; Aschwanden 1998), both of which become efficient with enhanced pitch-angle scattering, rather than weak pitch-angle diffusion that we needed to explain the observed morphology. We therefore do not consider, in this paper, the hypothesis that the observed spectral evolution is entirely controlled by acceleration, although such a possibility cannot be excluded in general.

### 3. MODELING

We consider a model in which electrons are injected into a specific magnetic loop and evolve in the energy and pitch-angle space as influenced by Coulomb collisions and magnetic mirroring. We present our modeling of the Coulomb collisions in § 3.1 and magnetic mirroring in § 3.2 and our method of calculating continuous injection and microwave emissions in § 3.3.

#### 3.1. Coulomb Collisions

The effects of Coulomb collisions on high-energy electrons are loss of energy and diffusion of pitch angles. Under our assumption that the trap density is uniform in space and time, the energy change of an electron under Coulomb collisions (ignoring the second-order term) depends only on the total path traversed by the electron since its injection (or equivalently, on time  $t$ ) and is independent of its pitch angle. The energy-dependent variation of electrons can be described by analytic expressions (see eqs. [1] and [2]), whereas modeling of pitch-angle variation requires incorporation of a detailed magnetic field structure. In the present approach, we start from the expressions for the energy-dependent Fokker-Planck solution and use them in building the pitch-angle-dependent part of the solution in combination with a specific magnetic field structure.

The Coulomb energy loss of an electron is described by  $\dot{\gamma} = -\alpha_C \beta^{-1}$  (Gould 1972), where  $\gamma$  is the Lorentz factor of the electron,  $\beta = v/c$ , and  $\alpha_C \approx 6 \times 10^{-3} n_{10}$ , with  $n_{10}$  the ambient density in units of  $10^{10} \text{ cm}^{-3}$  (see, for a definition, Hamilton, Lu, & Petrosian 1990). In this paper we use  $\gamma$  instead of  $E = \gamma - 1$  because the gyrosynchrotron emission is expressed in terms of  $\gamma$  (eq. [6]). The solution to this equation gives the relationship between the energy of an electron at time  $t$ ,  $\gamma(t)$ , and its energy at the time of injection,  $\gamma_0$ , as

$$\begin{aligned} [(\gamma_0^2 - 1)^{1/2} + \arcsin(1/\gamma_0)] \\ = [(\gamma^2 - 1)^{1/2} + \arcsin(1/\gamma)] + \alpha_C t. \end{aligned} \quad (1)$$

This expression (in different forms) is given in MacKinnon (1986) and Lu & Petrosian (1988). Leach & Petrosian (1981) give a relationship between two energies separated in distance,  $x(t) = \int_0^t \beta c dt$ , which is also equivalent to equation (1) in the present context. In this case, the electron number

density in energy space  $N(\gamma, t)$  will evolve from the distribution at the injection time  $N_0(\gamma_0)$  according to

$$N(\gamma, t) = \frac{\beta}{\beta_0} N_0(\gamma_0), \quad (2)$$

where  $\beta$  and  $\beta_0$  refer to time  $t$  and  $t = 0$ , respectively. This Fokker-Planck solution can be found in many places (Leach & Petrosian 1981; MacKinnon 1986; Lu & Petrosian 1988). Leach & Petrosian (1981) give an equivalent expression but in terms of  $N(E, x)$ . The solution of MacKinnon (1986) includes the effect of time-dependent change of the trap density, i.e.,  $n(t)$ . Lu & Petrosian (1988) give a more general solution with both energy and pitch-angle dependence.

The change of pitch-angle distribution is described in terms of the diffusion coefficient,  $D_{\mu\mu}$ , and the drift rate,  $\dot{\mu}$ , which are given as (e.g., Hamilton et al. 1990)

$$\begin{aligned} D_{\mu\mu} &= 4\alpha_C(1 - \mu^2)\beta^{-3}\gamma^{-2} \\ \dot{\mu}_C &= -8\alpha_C\mu\beta^{-3}\gamma^{-2}, \end{aligned} \quad (3)$$

where  $\mu$  is the cosine of the electron pitch angle and the subscript in  $\dot{\mu}_C$  signifies that it is due to Coulomb collisions, to distinguish it from that due to magnetic mirroring. As can be seen here, the mathematical complexity lies in the fact that pitch-angle variation depends not only on time and distance but on pitch angle itself, which undergoes cyclic variation while bouncing within the magnetic bottle. A simplification we use here is as follows: for events in which Coulomb collisions dominate the trap lifetime and this lifetime is much longer than the bounce time, the overall evolution is small within a single bounce and the electrons injected at the loop apex will come back to the loop apex, after bouncing, with the pitch angles only slightly different from those pertaining before the bounce. These negligible changes will, however, accumulate with time to become significant only after multiple bounces. We thus conveniently separate the evolution into two processes: a short-term evolution (of order one bounce time), which approximately follows adiabatic invariance, and a long-term evolution (of order the observed decay time) in which the secular variation is important. The former is simply described by the adiabatic invariance,  $d[(1 - \mu^2)/B]/dt = 0$  anywhere on the magnetic loop. Calculation of the secular term is still complicated, as it contains the periodic variation of  $\mu$  in each bounce cycle, which depends on the detailed magnetic field structure. We note that what we want is the time integrals of  $\dot{\mu}$  and  $D_{\mu\mu}$  rather than these quantities themselves, and so we consider the time integral of these quantities as the sum over bounces of the change integrated over each bounce cycle so that the mean  $\mu_0$  and the width  $\Delta\mu$  of the pitch-angle distribution at time  $t$  can be calculated from

$$\begin{aligned} \mu_0(t_m \leq t < t_{m+1}) &= \mu_0(0) + \sum_{i=1}^m \left[ \int_{t_{i-1}}^{t_i} \dot{\mu}_C dt \right] \\ \Delta\mu^2(t_m \leq t < t_{m+1}) &= \Delta\mu^2(0) + \sum_{i=1}^m \left[ \int_{t_{i-1}}^{t_i} D_{\mu\mu} dt \right], \end{aligned} \quad (4)$$

where  $m = (c/L_\mu) \int \beta dt$  is the number of bounces that the electrons have made since their injection at a specific time of observation  $t$ . Now in calculating the quantities within the brackets [ ], a given magnetic field structure of a loop

should be incorporated into it, which we will explicitly describe in § 3.2.

Once these two quantities are determined, we use them to calculate the pitch-angle-dependent part of the solution,  $P(\mu)$ , which is given by a Gaussian centered at  $\mu_0$  with width  $\Delta\mu$ :

$$P_\gamma(\mu)|_{s=0} = \frac{1}{\sqrt{\pi}\Delta\mu} \exp\left[-4\frac{(\mu - \mu_0)^2}{\Delta\mu^2}\right]. \quad (5)$$

$\mu_0$  are functions of  $(\gamma, t)$ . A Gaussian solution for the pitch-angle distribution has been used elsewhere. Leach & Petrosian (1981) and Lu & Petrosian (1988) found that such a Gaussian solution results in the small pitch-angle approximation. Miller & Ramaty (1989) used a Gaussian function for pitch-angle distribution in their Monte Carlo simulation. Our reason for having a Gaussian form of  $P(\mu)$  is that we concern ourselves only with quantities averaged over a bounce cycle, and a Gaussian gives a way of expressing the pitch-angle distribution undergoing a stochastic diffusion. Note that  $\mu$  in equation (5) merely represents an independent variable used for  $P(\mu)$  at the loop top whereas  $\mu$  in equation (3) represents the pitch angle of electrons associated with their trajectory of motion within a bounce.

Finally, we combine the energy-dependent solution (eq. [2]) and the pitch-angle distribution (eq. [5]) to represent the full solution as  $f(\gamma, \mu, t) = N(\gamma, t)P_\gamma(\mu)$  (cf. Lu & Petrosian 1988 as a more general approach). This assumes that the evolution of electron energy distribution can be determined independent of their pitch angles. This solution,  $f(\gamma, \mu, t)$ , corresponds to the electron distribution in phase space at the loop top at time  $t$  subject to the injection  $N(\gamma_0, 0)P_{\gamma_0}(\mu)$  made instantaneously at  $t = 0$ . The solution elsewhere in the loop can be found from the adiabatic invariance since we are including only the magnetic mirroring force to describe the transport effect during one transit time of electrons within a loop.

### 3.2. The Magnetic Mirroring

The effect of magnetic field variations on electron pitch-angle evolution arises from the integral of the  $\mu$  trajectory over a bounce cycle (see eq. [4]). For convenience, let us define two quantities:  $F \equiv \int_{t_i}^{t_i+T} \mu(t')dt'$  and  $G \equiv \int_{t_i}^{t_i+T} \mu^2(t')dt'$ , where  $t = t_{i-1}$  and  $T = t_i - t_{i-1}$  in the notation used in equation (4) and  $T$  is the time for one complete (forward and backward) bounce cycle. We also introduce a variable, the phase  $\psi$  within the bounce cycle defined as  $\psi = 1 - 4(t' - t)/T$  so that  $0 \leq \psi \leq 1$  for  $t \leq t' \leq t + T/4$ . Thus,  $\psi$  remains the same from bounce to bounce while  $T$  itself varies with time as  $\beta(t)$  does.  $F$  and  $G$  can be computed numerically for any form of  $B(s)$  using the adiabatic invariant condition. For this discussion, however, we instead examine specific forms of  $\mu(\psi)$ , so that  $F$  and  $G$  can be expressed in analytical form, and then determine the form of  $B(s)$  that results, where  $s$  is the arc distance measured along the loop from the loop top. Suppose that  $B(s)$  varies along a loop in such a way that it leads to the pitch-angle variation (approximately) in a form  $\mu(t) = \mu(\psi(t)) = \mu_0(1 - \psi^p)$ . We then have  $F = 4[p/(p+1)]\mu_0 T$  and  $G = 8p^2/[(p+1)(2p+1)]\mu_0^2 T$ . Our motivation for setting  $\mu(\psi)$  in such a form is that  $B(s)$  in real loops could well be approximated by polynomials of powers of  $s$ , which is, in turn, well approximated by the above form of  $\mu(\psi)$ . Considering the relationship between  $B(s)$  and  $\mu(s)$  under adiabatic invariance, one can

see that a smaller  $p$  in this expression gives a rather linear increase of  $B(s)$  from the loop top to the footpoints while a larger  $p$  gives a relatively slow variation of magnetic field around the loop top and a more rapid variation near the footpoints.

In Figure 2, we use this formulation to examine the effect of differing  $B(s)$  on electron pitch-angle diffusion. Here we create three hypothetical loops by choosing  $p = 1, 2, 3$ , corresponding to loops A, B, and C, respectively. If  $p = 1$ , a loop that has magnetic field strength straightforwardly increasing from the loop top to footpoints results. We suggest that  $p = 1$  would give a lower limit to  $p$  because, on most loops,  $B(s)$  will slowly increase near the loop top but vary more rapidly near the footpoints. The other limit, in which  $B(s)$  is nearly constant for a wide range of  $s$  around the loop apex and then rapidly increases only near the footpoints, can be considered. Here we simply choose  $p = 3$  for such a case. As we will show later (§ 4), we expect that  $p \sim 2$  would be typical for solar loops. Figures 2a and 2b show  $\mu(\psi)/\mu_0$  for three hypothetical loops with  $p = 1, 2, 3$  and the corresponding  $B(s)$ , respectively. Note that all of these loops have the same loop top to footpoint distance and loss cone angles. They differ only in the degree of magnetic field variation, which is what we wish to emphasize here.

Figure 2c shows the transit distance  $L_\mu = \int ds/\mu$  as a function of  $\mu$  for the three loops, which is needed for computation of  $T$  or  $m$  and thus that of  $\mu_0(t)$  and  $\Delta\mu^2(t)$  in equation (4). We note that these  $L_\mu$  are symmetric with respect to  $\mu = 0$  because we assumed that the same  $p$  applies to both sides of the loop, although these loops are asymmetric in terms of the physical lengths of each side. At  $\mu = 0$ ,  $L_\mu$  is not defined, and there we use  $L$  corresponding to an arbitrary short time interval times the velocity of electron  $v$  at that time. We do not think that this is a problem because, although  $L_\mu$  is not defined (as if the electron is frozen in space), time continues to advance and the pitch-angle diffusion and energy loss continue to occur so that things are not frozen in time as well. Figure 2d compares the integral quantities  $F$  and  $G$  for three loops, which are needed for computing  $\mu_0(t)$  and  $\Delta\mu^2(t)$  in equation (4). Here the two adjacent bars represent  $F$  (dark gray bars) and  $G$  (light gray bars), respectively. As this figure shows, the quantities  $F/T$  and  $G/T$  noticeably differ from loop to loop. However, such difference does not strictly affect the pitch-angle evolution in each loop as discussed below.

Figures 2e and 2f show, respectively,  $\mu_0(t)$  and  $\Delta\mu^2(t)$  as functions of time. Each curve is stepwise varying in time because of the model assumption (eq. [4]), with each step representing one bounce. Note that the size of the time step varies considerably, depending on the magnetic field structure. For a modest choice of  $p$  the time step is short enough compared with the observational timescale to be regarded as an essentially continuous change. We can see that, despite the vastly different variation of  $B(s)$  that we assumed, the integrated quantity differs only a small amount in the three loops, and so in terms of pitch-angle evolution the exact form of magnetic field variation in the loop plays only a small role. The difference between differing  $B(s)$  gets even smaller as time goes by because  $\mu_0$  itself approaches zero. Although there is a significant variation in the mean pitch angle  $\mu_0(t)$ , this distinction becomes less important as the beam broadens with time. We conclude that the exact form of the magnetic field variation,  $B(s)$ , does not greatly affect the evolution of the particles. It should be

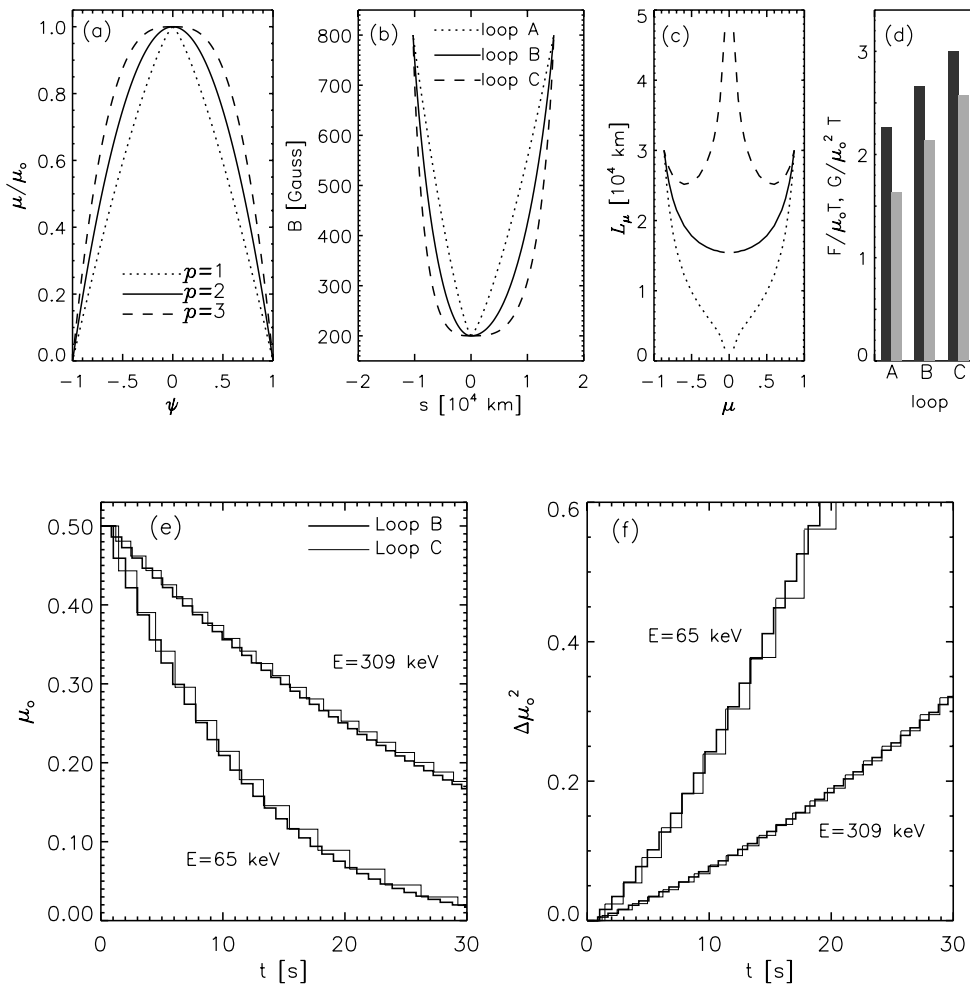


FIG. 2.—Magnetic loop and pitch-angle evolution. (a) Pitch-angle  $\mu$  variation as a function of the phase  $\psi$  in the bounce cycle (see text for definition of  $\psi$ );  $p = 1$  (dotted curve),  $p = 2$  (solid curve), and  $p = 3$  (dashed curve) are used to create three different hypothetical loops (A, B, and C, respectively). (b) Magnetic field strength as a function of arc distance,  $s$ , of the three hypothetical loops. The loops may be asymmetric as shown. (c) Transit distance  $L_\mu$  calculated as a function of mean pitch angle. (d) The two integrals  $F/\mu_0 T$  (dark gray bars) and  $G/\mu_0^2 T$  (light gray bars) calculated for the loops (see text for definition of  $F$  and  $G$ ). (e) Time variation of the mean pitch angle,  $\mu_0$ , as observed at two different energies. The time steps are vastly different for different loops because of differing  $L_\mu$ . The curves with the shorter and the larger time steps are those in loops B and C, respectively.  $n_{10} = 0.5$  is used. (f) Time variation of the width of the pitch-angle distribution,  $\Delta\mu_0^2$ .

noted that this conclusion would change if the electron density varies significantly with position in the loop.

Another effect of a specific magnetic structure of a loop that should be included in this model is the size of the loss cone angle, which affects the number of microwave-emitting electrons remaining in the trap at a given time. In fact, the time variation of trapped versus precipitating electrons is not only a matter of the loss cone angle size but in the case of a narrow, beamed injection also involves the angle of the injected beam  $\mu_0(t = 0)$  relative to  $\mu_L$ . For illustration, here we discuss the problem only with a simple case, an instantaneous injection in a specific form, and later (in § 4.2) we further discuss the effect of beam properties.

In Figure 3, we consider injection in the power-law form  $N_0(\gamma, 0) \sim (\gamma - 1)^{-\delta}$  and with  $\mu_0(\gamma, 0) = 0.5$ ,  $\Delta\mu(\gamma, 0) = 0.26$ , and  $n_{10} = 1.0$ . The left panels in Figure 3 show evolution of the electron distribution  $f(\gamma, \mu, t)$  on the  $(\gamma, \mu)$ -plane at three different times:  $t = 0$ ,  $t = 5$  s, and  $t = 20$  s from top to bottom. The evolution occurs in both pitch angle and energy space. As the evolution progresses in energy space, the maximum of  $f(\gamma, \mu, t)$  moves to progressively higher

energy (10, 80, and 200 keV in the three selected times) because of the fact that energy loss under Coulomb collisions is more effective at lower energies. In terms of pitch angle, we can see that the beam diffuses (broadens) with time and also the mean beam drifts toward  $\mu = 0$  because of dynamical friction. Toward higher energies ( $\geq 1$  MeV) the electrons tend to remain unchanged in both energy and pitch angles although the total number itself decreases. For clarity, the middle panels show the pitch-angle evolution at two different energies. At a low energy it is quickly isotropized, but at high energy it does not fill the entire  $\mu$  range until much later. The right panel in Figure 3 shows the spectrum of electron density in energy, which is obtained by integrating  $f(\gamma, \mu, t)$  with respect to pitch angle for different loss cone angles. We show  $\mu_L = 1.0$  (a perfect trap) and  $\mu_L = 0.7$  in order to see the effect of precipitation. Note that the difference between the two cases is initially small because the pitch-angle distribution is not fully broadened to reach the loss cone and precipitation has not occurred, but later the difference between two  $\mu_L$  loops increases. The time behavior and the energy dependence of the precipi-

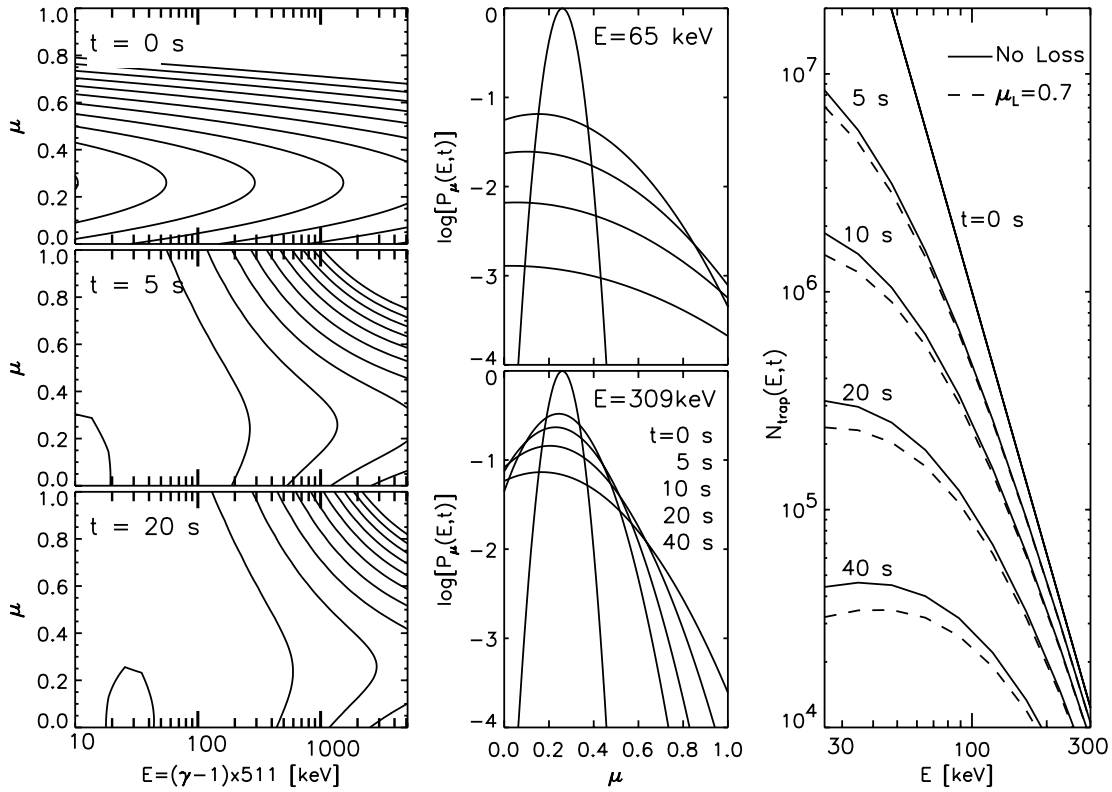


FIG. 3.—Evolution of electrons after instantaneous injection into magnetic loops. *Left*: Electron distributions on a two-dimensional plane with axes of energy  $E$  and cosine of pitch angle  $\mu$  at three times:  $t = 0, 5$  s, and  $20$  s from top to bottom. Injection in the form of  $N(\gamma) \sim (\gamma - 1)^{-4}$  with a narrow beam distribution  $P_\mu(\mu) \sim \exp\{-[(\mu - 0.5)/0.26]^2\}$  is used together with a trap density of  $n_{t,0} = 1.0$ . *Middle*: Evolution of the pitch-angle-dependent part of the electron number density at two different energies,  $65$  and  $309$  keV. As time goes by, its width increases and the central pitch-angle cosine moves to zero. From these, we calculate the trapped component of electrons by integrating  $f(\gamma, \mu, t)$  with respect to the pitch-angle cosine from zero to the cosine of the loss cone angle,  $\mu_L$ . The results are shown in the right panel. The cases of a perfect trap (*solid curves*) and a trap with a loss cone of  $\mu_L = 0.7$  (*dotted curves*) are shown.

tation in this model differs from that resulting from the ideal trap and precipitation model of Melrose & Brown (1976).

As an aside we note that transit distance  $L_\mu$  and asymmetry of the magnetic loop have an insignificant effect in this problem. Although the number of bounces  $m$  made until time  $t$  will increase for a loop with shorter  $L_\mu$ , the time spent per bounce,  $\Delta t$ , is shorter with a smaller  $L_\mu$ . The net amount of pitch-angle change, since it is proportional to  $m\Delta t$ , will make little difference among loops with differing  $L_\mu$ . The loop asymmetry does not matter here because we are counting the sum of electron pitch-angle evolutions in both sides of the loop. Indifference to these two quantities is largely due to the fact that we are dealing with an electron evolution that changes significantly only over multiple bounces but not on a timescale shorter than the transit time.

### 3.3. Calculation of Continuous Injection and Microwave Radiation

A final important step is to generalize the above solution to include continuous injection, whereby electron acceleration continues over a finite time. This we do by fully numerical convolution of the instantaneous injection solution  $f(\gamma, \mu, t)$  with the injection time profile  $q(t)$  in some prescribed form. Specifically, we make multiple copies of  $f(\gamma, \mu, t)$  and shift them to other times sufficiently closely spaced to ensure accuracy in the integration. Each copy is then multiplied by the injection function  $q(t)$  at the corresponding time, and the result is integrated to yield the convolution. Such convolution is repeated at each energy and

pitch-angle grid point. Our convolution algorithm has been checked against the analytic expression of Melrose & Brown (1976). As a fully numerical scheme, this method can handle arbitrary functions of electron distribution and injection time profile.

We compute the microwave emission from the resulting electron population under the assumption that the emission is due to gyrosynchrotron radiation. We compute only the emissivity, which corresponds to the optically thin spectrum and depends directly on the electron distribution, to avoid complication due to absorption geometry. This limits the application to radio frequencies above the turnover in the spectrum, which is sufficient for our purposes, although a more general microwave calculation could be used to include absorption if that is needed.

The theoretical expression for gyrosynchrotron emissivity is (Ramaty 1969)

$$j_\nu(t) = 2\pi \int_1^\infty d\gamma \int_{-1}^1 d\mu f(\gamma, \mu, t) \eta(\nu, \theta, \gamma, \mu), \quad (6)$$

where  $\eta$  is the gyrosynchrotron emissivity for a single electron and  $f(\gamma, \mu, t)$  in this expression is the electron number density in phase space for continuous injection.  $\eta$  contains a delta function whose argument represents the gyroresonant condition (see eq. [14] of Ramaty 1969)

$$\nu - \frac{sv_b}{\gamma} - n_\pm v\beta\mu \cos \theta = 0, \quad (7)$$

where  $s$  in this expression is the harmonic number;  $\nu$  is the radiating frequency;  $\nu_b$  is the gyrofrequency ( $=2.8 \times 10^6 B$ );  $n_{\pm}$  is the index of refraction, which is close to unity at the frequencies that concern us here; and  $\theta$  is the viewing angle of the magnetic field vector with respect to the line of sight. Thus, the resonance condition limits the harmonic range available for gyrosynchrotron emission depending on the magnetic field ( $B$ ,  $\theta$ ) and the number of electrons  $f(\gamma, \mu)$  at the energy and pitch angle corresponding to the harmonic. The integration over  $d\mu$  will also be strongly affected by the location of the loss cone angle. For this reason, we expect that microwave emission should be sensitive to precipitation and to any anisotropy in pitch-angle distribution of the electrons as well as to magnetic fields.

Because of the context of the present model the following points need to be considered in calculating the microwave spectrum. We have assumed that the spatial distribution of electrons at time  $t$  can be represented by electron motion within a bounce cycle  $[t - T/2, t + T/2]$ . Therefore, both the forward and backward motions during the bounce are used in the present formulation to represent the spatial structure of a magnetic trap so that it makes sense to use the average,  $P_{|\mu|} = (P_{+\mu} + P_{-\mu})/2$ . In addition, an asymmetric loss cone angle is not meaningful because the present model also assumes weak diffusion, in which case the loss cone in the side of the loop with higher  $\mu_L$  will be almost vacant. Consequently, the smaller  $|\mu_L|$  would actually determine the effective precipitation and can be used in counting the precipitating population.

#### 4. ELECTRON INJECTION VERSUS MICROWAVE RADIATION

We here investigate the relationship between the injection parameters and the resulting microwave spectral variations that our model predicts. In order to calculate microwave radiation, the magnetic field distribution in the trap must also be specified. For illustration, we calculate the radiation from a single point on the trap, the magnetic loop apex, although the microwave spectrum elsewhere in the loop can be calculated in a straightforward manner. We use particular values:  $B_0 = 200$  G,  $\theta = 50^\circ$ , and  $\mu_L = 0.6$ , which correspond to the case of the observed loop that we will be dealing with in § 5. We assume that the temporal variation of the instantaneous injection spectrum occurs only in amplitude but not in energy or pitch-angle distribution; i.e.,  $q(t)$  (defined in § 3.3) does not depend on energy or pitch angle. We adopt this assumption not merely for convenience but because of the observed invariance of the microwave spectral index during the early rise phase (see Fig. 8). A main focus of this modeling is then to test whether the observed spectral index variation afterward can be explained solely in terms of Coulomb collisions and magnetic mirroring without variation in the injection energy distribution.

##### 4.1. Injection Time Profile

The functional form of the injection time profile will remain largely hypothetical yet may nevertheless affect the results strongly. We find in the literature three types of injection profile that have been used: a parabolic type (Vilmer et al. 1982), a triangular type (Mel'nikov 1994; Mel'nikov & Magun 1998), and an exponential type (Gary & Tang 1985). To express them in a way that gives a maximum value of unity at  $t = t_0$  but with different charac-

teristic timescales, they are, respectively,

$$\begin{aligned} q_1(|t - t_0| \leq \tau_1) &= (t - t_0 + \tau_1)(\tau_1 - t + t_0)/\tau_1^2 \\ q_2(|t - t_0| \leq \tau_2) &= 1 - |t - t_0|/\tau_2 \\ q_3(t) &= \exp(-|t - t_0|/\tau). \end{aligned} \quad (8)$$

To normalize each timescale to yield equal total fluence in each case,  $\tau_1 = 1.5\tau$  and  $\tau_2 = 2\tau$ . These time profiles are all set to be symmetric with respect to the maximum injection time,  $t_0$ . Although there is no physical ground for such symmetry and an asymmetric time profile could be more realistic in general, we note that, for the purpose of model fitting to the observation, the decaying part is less important than the rising part as long as the electrons survive longer than the injection decay time, which is the case in the present study. Therefore, whether the time profile is symmetric or asymmetric is not so critical to the present modeling, and we keep the symmetric profile in order not to introduce an additional, nonessential parameter.

In Figure 4, we show the above three injection profiles and compare the resulting radiation at 10 GHz in each case. First of all, note that the radiation fluxes from three different injection time profiles eventually converge to the same decay amplitude and timescale. This is because the decay is determined by the integrated number of electrons under the same physics of Coulomb collisions. To reflect the integrating nature of the trap, the point of fastest rise in flux occurs at the peak of the injection in each case, which may be used to infer the time of injection maximum from the observed microwave radiation. At the impulsive phase, however, the parabolic profile results in the steepest increase and the largest radiation output whereas the exponential profile yields the smallest and the triangular one, the intermediate. This is expected because the parabolic type results in the largest number of electrons in the shortest time, before decay due to collisions can become appreciable.

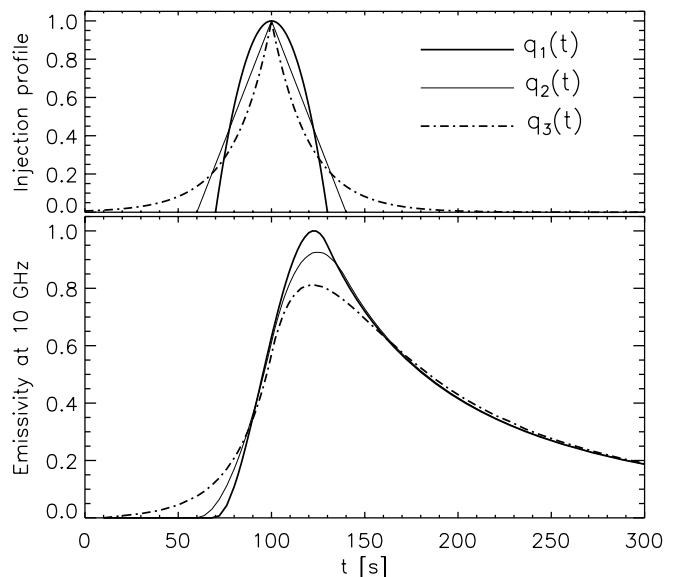


FIG. 4.—Relationship between the (top) injection time profiles and (bottom) time profiles of the resulting gyrosynchrotron emissivity. In the upper panel,  $q_1$ ,  $q_2$ , and  $q_3$  correspond to parabolic, triangular, and exponential functions, respectively, normalized to yield equal total injection fluence (see text). The resulting radio emissions are shown in the lower panel.

This exercise shows that some basic properties of the injection time profile can be constrained by the microwave time profiles observed at the rise phase and the impulsive phase and need not be arbitrarily assumed. From this result we note again that the assumed symmetry of the injection time profiles is nonessential.

4.2. Injection pitch-angle Distribution

We investigate the role of injection beam parameters on the subsequent evolution of electrons and the resulting radiation under an instantaneous injection in Figure 5 and a continuous injection in Figure 6. In both figures, the small panels on the left show time profiles of the electron number density  $f(\gamma, \mu, t)$  at three energies (48 keV, 420 keV, and 1.1 MeV

MeV) and two pitch-angle cosines ( $\mu = 0.3$  and  $0.7$ ). Here we try five combinations of variations in the initial pitch-angle parameters: widths  $\Delta\mu(t = 0) = 0.09, 0.26,$  and  $0.5$  and mean pitch angles  $\mu_0(t = 0) = 0$  and  $0.5$ . The large panel on the right shows monochromatic flux density at 13 GHz calculated from the electron distribution over the entire energy and pitch-angle phase space. A trap density  $n_{10} = 0.5$  and single power law  $\delta = 7$  is used throughout. Note that all time profiles shown here are normalized to unity in order to focus on the relative timing of the peak of electrons and radiations relative to injection.

For the instantaneous injection case shown in Figure 5, we normally expect that electron and microwave radiation would be simply a decreasing function from its maximum at

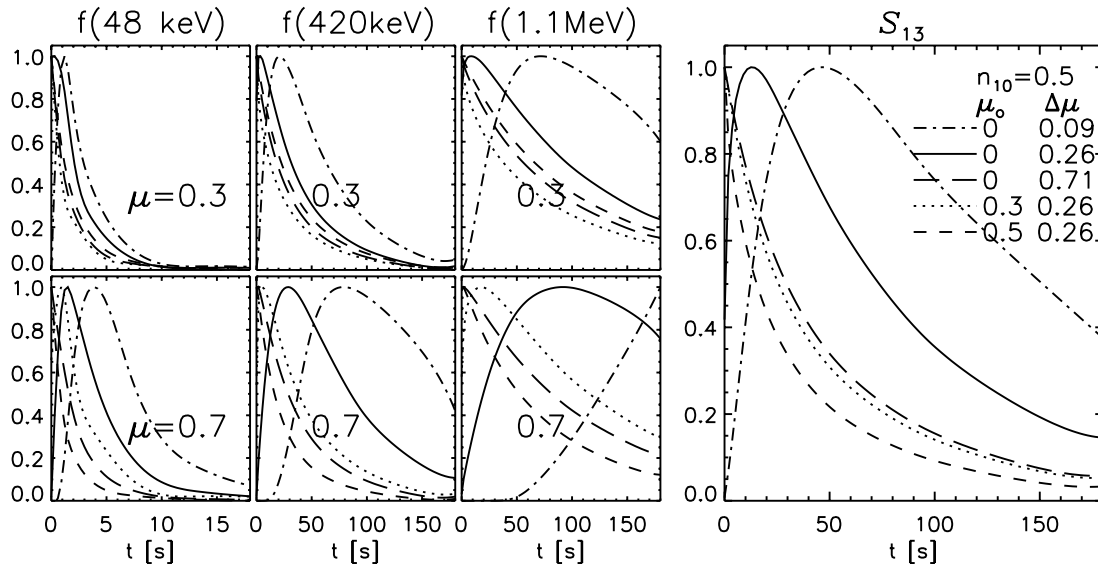


FIG. 5.—Relationship between the injection beams and radiation time profiles under an instantaneous injection. We vary either the beamwidth  $\Delta\mu$  at a fixed  $\mu_0 = 0$  or the injection pitch angle  $\mu_0$  at a fixed beamwidth  $\Delta\mu$ .  $n_{10} = 0.5$  is used for all cases. The small panels on the left show time profiles of electrons at three energies (48 keV, 420 keV, and 1.1 MeV) and two pitch angles ( $\mu = 0.3$  and  $0.7$ ). The larger panel on the right shows the resulting microwave flux time profiles using these model parameters. Note that all time profiles of the  $f(\gamma, \mu, t)$  and the radio flux are normalized to unity in order to emphasize the relative time variations.

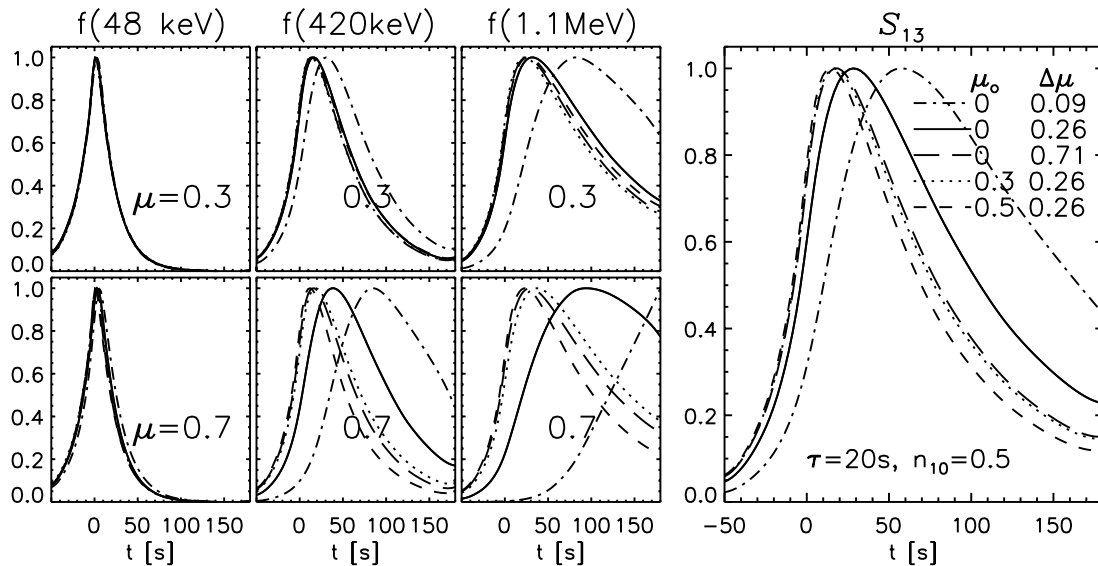


FIG. 6.—Same as Fig. 5 but for a continuous injection case. An exponential time profile with  $\tau = 20$  s is used.

the injection time ( $t = 0$ ). Figure 5 shows that this is true only at some combination of  $\mu$  and  $\Delta\mu$ , in general those with initially broad pitch-angle distribution and at low energies. If, on the other hand, it started from an initially narrow pitch-angle distribution, a delayed maximum of electrons and radiation results relative to the instantaneous injection. This is because it takes a longer time to fill all pitch angles required for resonance (see eq. [7]). Of importance for the present study, the decay time is also extended in such a case. These trends increase toward higher electron energy because pitch-angle scattering and drift under Coulomb collisions take a longer time at higher energies (see eq. [3]). As an extreme case,  $f(E = 1 \text{ MeV}, \mu = 0.7, t)$  is still rising during the entire period. The microwave time profile is a combination of those over a wide range of energies and pitch angles, and the result shown in the rightmost panel shows that the maximum of  $j_{\nu}(t)$  from a narrower beam with  $\Delta\mu(t = 0) = 0.09, 0.26$  is delayed by  $\sim 40$  s with respect to the injection time, whereas there is no time delay for cases with a more isotropic beam  $\Delta\mu(t = 0) = 0.26, 0.71$  at  $\mu_0 = 0.3, 0.5$ .

In Figure 6, we extend the result to include continuous injection in the form of an exponential  $q(t)$  with  $\tau = 20$  s. The trend of delayed peak and extended decay with narrower injection beamwidth  $\Delta\mu$  seen in the previous case of instantaneous injection (Fig. 5) is relatively unchanged. One main difference is that we now have a smoothly rising profile in the rise phase determined by the assumed time profile of injection  $q(t)$ . At a low energy (48 keV), all time profiles closely follow the injection time profile  $q(t)$  regardless of the form of injection beams ( $\mu, \Delta\mu$ ), not only because electrons are quickly isotropized at the low energies but because they also die quickly. At higher energies, this trend changes; now under continuous injection, even the near-isotropic injection case shows a finite delay with respect to the time of maximum injection due to increasing electron lifetime with energy. The energy-dependent time delay has been well known in hard X-ray observations since Bai & Ramaty (1979), but the  $\mu$ -dependent time delay is new in this study and unique for microwave radiation because of its great sensitivity to electron pitch angle.

The results presented in Figures 5 and 6 show that the peak of the resulting microwave radiation is further delayed in the case of a narrow beamed injection compared with an isotropic injection case even at the same trap density. Thus, the trap density is not the only factor in determining the time delay and the decay time profile as far as microwave radiation is concerned.

While the variation with  $\Delta\mu$  is easily understood, there is one complication about the variation with the initial mean pitch angle  $\mu_0(t = 0)$ . As  $\mu_0$  increases (becoming parallel to the magnetic field), the dependence of the resulting radiation on  $\mu_0$  decreases. That is, the effect of the narrow beam is much reduced when  $\mu_0$  is located close to the loss cone. This is due to the fact that the Gaussian distribution is truncated at  $\mu_L$ , resulting in a corresponding increase in the precipitational loss. Significant truncation has an effect on the decay time and delay of the peak similar to that of the isotropic injection. It therefore appears that the above-mentioned effect of  $\mu$ -dependent time delay is sensitive to  $\mu_0$  and that  $\mu_0 \sim 0$  should be chosen in order to have a significant effect of a narrow beam. Hereafter we consider only  $\mu_0(t = 0) = 0$ , corresponding to the injection perpendicular to the magnetic loop.

### 4.3. Injection Energy Distribution

The energy distribution of injected electrons will also affect the time evolution of the electron distribution and thus that of resulting radiation. As can be seen from equation (1), the number of electrons at a given energy  $\gamma$  and time  $t$  is determined by the number at the energy  $\gamma_0$  that they had at the time of injection. Therefore, electrons injected with a harder energy distribution will decay more slowly than those with a softer initial energy distribution if other conditions are identical. While the effect of injection energy distribution is obvious, it is still necessary to know, for the purpose of modeling, how this effect is eventually combined with the effects of other parameters ( $n_{10}, \tau, \Delta\mu$ ) on the microwave spectral variation.

In Figure 7, we calculate a microwave spectral index defined by fluxes at two frequencies, 10.0 and 13.2 GHz, i.e.,  $\Gamma \equiv -\log [j(13.2 \text{ GHz})/j(10.0 \text{ GHz})]/\log (13.2/10.0)$ , for a fixed electron hardness  $\delta = 7$  in combination with other parameters ( $n_{10}, \tau, \Delta\mu$ ). Again an exponential injection time profile  $q(t)$  is used. As a characteristic behavior, the spectral index  $\Gamma$  is nearly constant from the beginning of injection up to the time of maximum injection and then decreases more rapidly afterward. Thus, this time behavior of spectral index gives a second method to infer the time of maximum injection, in addition to the aforementioned inflection point of the flux time profile in the rise phase (see § 4.1). In addition, we note the following. (1) Increasing the ambient density (*solid lines* vs. *dotted lines*) results in an initially harder spectrum (smaller  $\Gamma$ ) and faster decay of the spectral index itself. (2) Increasing the injection time has the opposite effect; it also makes the initial spectrum harder, but the emission decays more slowly. (3) Narrowing the beamwidth, the microwave spectrum gets steeper overall but has a similar time profile—as a result it is like shifting the same profile vertically.

Alternatively, it can be more desirable to determine the injection energy distribution (rather than leaving it as a free parameter) by matching the observed spectral index  $\Gamma$  at one particular time (e.g., the initial rising time), for a given set of other parameters ( $n_{10}, \tau, \Delta\mu$ ). Thus, we can test the model parameters by looking at whether the model continues to match the observation as it evolves through the decay phase. Figure 7b shows the results when we choose a  $\delta$  that predicts  $\Gamma = 7.1$  at  $t = 0$  for the same set of other parameters used in Figure 7a. As we expect, the decay time tends to increase when a lower trap density  $n_{10}$  or a longer injection time  $\tau$  is used. Not so obviously, varying the injection beamwidth  $\Delta\mu$  under the same set of other parameters leads to an insignificant difference in the spectral index  $\Gamma(t)$ . This is because a different electron hardness  $\delta$  can be chosen to counteract the effect of the different  $\Delta\mu$ , to yield a spectral index,  $\Gamma(t)$ , that evolves similarly. However, the evolution of the resulting monochromatic flux,  $S_{\nu}(t)$ , depends strongly on the electron hardness  $\delta$  and cannot be fit by multiple combinations of  $\delta$  and  $\Delta\mu$ . Therefore, the spectral index variation  $\Gamma(t)$  and the flux variation  $S_{\nu}(t)$  are complimentary measurements that provide ideal constraints for modeling microwave spectral observations.

In summary, our model investigation suggests that the form of injection time profile and the injection energy distribution can be determined from microwave spectral observations to some extent. In particular, the characteristic spectral index variation of microwaves in the rise phase can

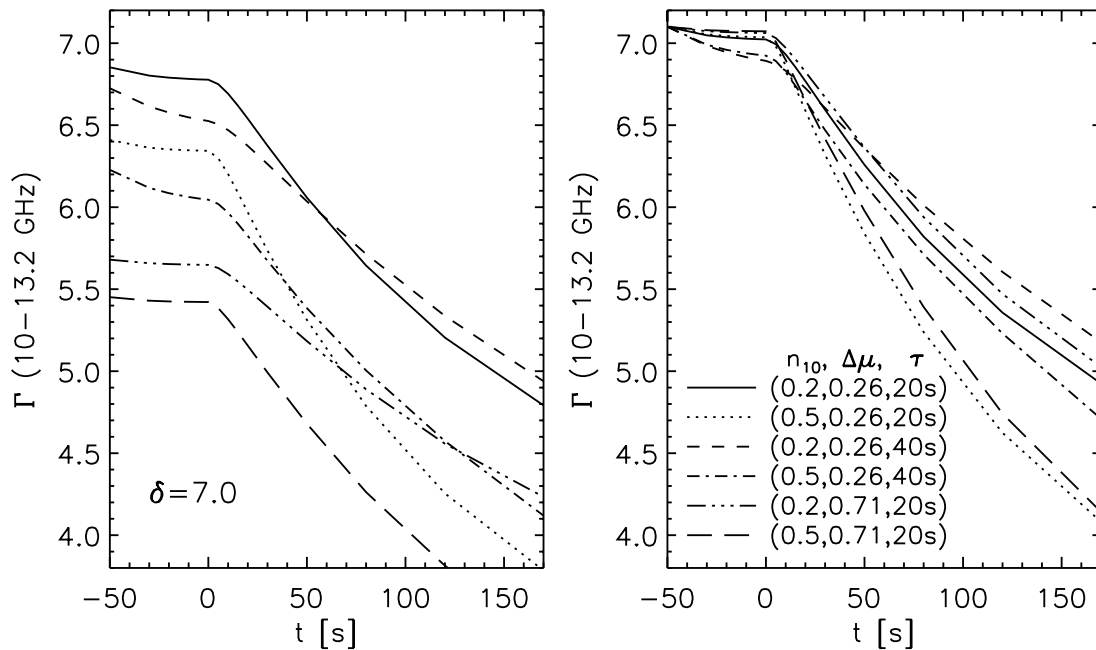


FIG. 7.—Relationship between the injection electron hardness and the microwave spectral index. The spectral index  $\Gamma$  is defined by emissivities at 10 and 13.2 GHz and calculated as a function of time for various sets of model parameters ( $n_{10}$ ,  $\Delta\mu$ ,  $\tau$ ). In the left panel,  $\Gamma$  is computed for a fixed electron hardness  $\delta = 7$ . In the right panel,  $\delta$  is adjusted to give rise to a common  $\Gamma$  at  $t = -50$  s for each set of model parameters.

be used to locate the time of maximum injection, which has otherwise been regarded as an unknown quantity. However, the injection beamwidth is found to play a crucial role in microwave spectral evolution, and it is thus necessary to include this parameter, along with the trap density and injection timescale, in modeling a given microwave spectral observation.

##### 5. APPLICATION TO THE MICROWAVE OBSERVATION

We now compare this model with the total power spectra of the microwave bursts described in § 2. The main observational constraints that we will use here are the time profile of the spectral index  $\Gamma$  from two frequencies, 10.0 and 13.2 GHz (as defined in § 4.3) and a relative time profile at 10 GHz,  $S_{10}$ . Matching these two quantities is equivalent to matching flux at two frequencies simultaneously. However, matching the spectral index and the flux at a single frequency allows a more systematic search for the solution. The observed time profiles of  $\Gamma$  and  $S_{10}$  are shown as crosses in each panel of Figures 8 and 9. In addition, we determine the time of maximum injection from the distinct change in spectral variation, from nearly constant spectral index to monotonic decrease (see Fig. 7), and set this to a reference time  $t = 0$  in Figures 8 and 9. In addition, the exponential form of injection profile (see Fig. 4) is chosen, again, based on observation. Finally, we consider the magnetic field variation of the flaring loop as follows: in the companion paper (Fig. 4 of Lee et al. 2000) we have determined the field strength distribution of the loop by comparing a *Yohkoh/SXT* image with a force-free field extrapolation from the photospheric fields. From the resulting  $B(s)$  along the loop we determine  $p = 2.0$  as a measure of the magnetic field variation (defined in § 3.2), which leads to  $F = 2.67\mu_0 T$  and  $G = 2.13\mu_0^2 T$ . Calculation of the radiation,  $j_r(t)$ , is made using magnetic fields at five points on the trap:  $(B, \theta) = (310 \text{ G}, 82^\circ)$ ,  $(260 \text{ G}, 64^\circ)$ ,  $(200 \text{ G}, 50^\circ)$ ,  $(260, -18^\circ)$ , and  $(310 \text{ G}, -32^\circ)$ , and  $j_v(t)$  from the

five points are then summed to yield the total flux. From the magnetic field model, we could also determine the loss cone angle cosine  $\mu_L = 0.61$  at the loop top. Hence, we proceed to do a model fit with a reduced set of free parameters: ( $n_{10}$ ,  $\tau$ ,  $\Delta\mu$ ).

We first consider an injection with a broad pitch-angle distribution, in which case the result is sensitive to only two parameters:  $n_{10}$  and  $\tau$ . In Figure 8 we compare the observation with model predictions made with  $\Delta\mu(t=0) = 0.7$  while varying  $n_{10}$  and  $\tau$ . The upper three panels show the flux at 10 GHz, and the lower panels show the spectral index variation. From left to right the trap density is increasing, and in each panel three different injection times are used. We can see that with a lower density we can better reproduce the 10 GHz time profile, but it yields a spectral index variation that is too slow, inconsistent with observation. On the other hand, with a higher density we can fit the spectral index variation  $\Gamma(t)$  but the flux  $S_{10}(t)$  falls too quickly. No combination of ( $n_{10}$ ,  $\tau$ ) that can reproduce  $\Gamma(t)$  and  $S_{10}(t)$  simultaneously could be found.

In Figure 9 we allow the initial beamwidth to vary and search for a set of parameters, ( $n_{10}$ ,  $\tau$ ,  $\Delta\mu$ ), that best reproduces the observation. To enable a systematic search for the best-fit parameters, we define a quantity  $\chi^2 = \sum_i [(y_{\text{model}}^i - y_{\text{obs}}^i)/y_{\text{obs}}^i]^2$  as a measure for goodness of the fit. Here  $y_{\text{obs}}^i$  represents either  $\Gamma$  or  $S_{10}$  observed at time  $t_i$  (22 time intervals) and  $y_{\text{model}}^i$  give the corresponding values predicted by the model. The left panels of Figure 9 show  $\chi^2$  calculated on two-dimensional space of ( $n_{10}$ ,  $\tau$ ) at each selected  $\Delta\mu$ . Here the contours are decreasing inward, and the cross marks the minimum of  $\chi^2$  at each  $\Delta\mu$ . Although the minimum can be found for each  $\Delta\mu$ , the overall minimum  $\chi^2$  is found for  $\Delta\mu(t=0) = 0.26$ . In order to see how good the fit actually is, we compare, in the right four panels, the model predictions with observation for the set of ( $n_{10}$ ,  $\tau$ ) that gives minimum  $\chi^2$  at the given  $\Delta\mu$ . In progressing from a highly beamed to a near-isotropic injection, there is a

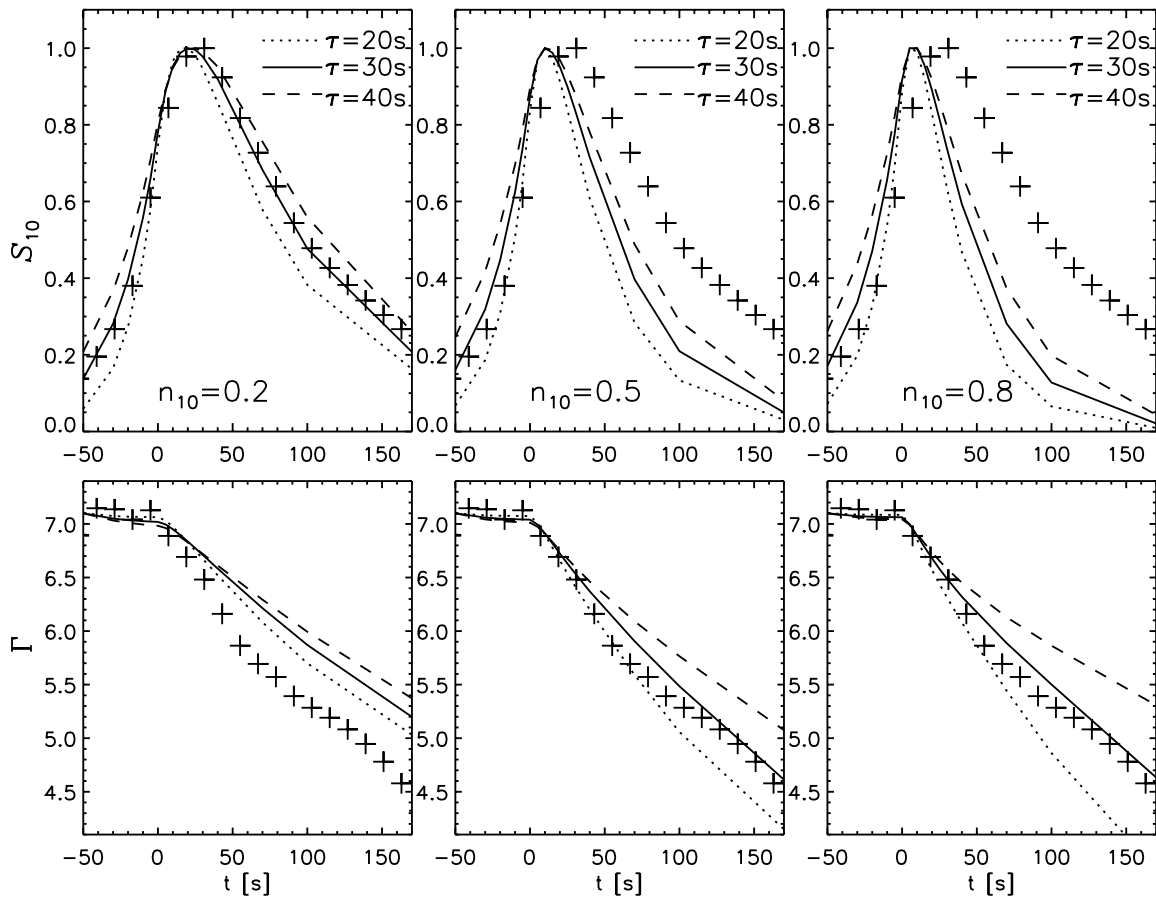


FIG. 8.—Model fit to the microwave observation under the hypothesis of near-isotropic injection. The lines are model fits and symbols are observed quantities during the 1993 June 3 flare. These are (*top*) flux at 10 GHz and (*bottom*) spectral index as a function of time.  $t = 0$  is set to the time of the maximum injection. The model trap density increases from the left to right panels, and in each panel three different injection times are used.

trend that the minimum  $\chi^2$  is found at lower density  $n_{10}$  and shorter  $\tau$ . However, in the case of the near-isotropic injection [ $\Delta\mu(t=0) = 0.71$ ], even the best fit is not really good in the sense that the spectral slope is a bit less rapid and the flux is a bit more rapid (cf. Fig. 8, *middle panels*), which again shows that the isotropic assumption does not work for the present observation.

The set of parameters that give the minimum  $\chi^2$  under our model hypothesis is  $\tau = 32$  s,  $n_{10} = 0.41$ ,  $\Delta\mu(t=0) = 0.26$ . The latter corresponds to  $\Delta\theta(t=0) \approx 30^\circ$ . This result indicates that this particular event involves injection of highly beamed electrons near vertical incident angle, with low density in the trap and with an injection time that is much shorter than the overall lifetime of the burst.

This conclusion of a narrow-beamed injection was reached under the assumption that the temporal variation of the microwave spectrum is due solely to electron evolution in phase space. To consider other possible effects that could affect the microwave spectral variation, we can think of (1) temporal variation of source area and (2) ambient density (cf. MacKinnon 1986), among others. Concerning case (1), we note that we use optically thin frequencies in order to eliminate any source size effects at a given time, but the source may contain an unresolved optically thick core, especially at 10 GHz. If such a source becomes progressively optically thin late in the burst (because of the decreasing number of accelerated electrons), its time profile will be

delayed with respect to 13.2 GHz, and the spectrum will soften with time, opposite to the behavior we observe. Concerning case (2), the trap density may have increased with time because of a process known as chromospheric evaporation. This will increase the rate of Coulomb collisions and cause the spectral index to harden more rapidly compared with the case of constant density. However, this will also result in more rapid decay of flux, which makes it difficult to explain the longevity of the burst. Thus, neither of these effects changes our conclusion concerning the need for a nonisotropic (beamed) injection, although ignoring these effects may increase the uncertainty in the best-fit parameters from a quantitative standpoint.

## 6. THE HARD X-RAY COUNTERPART

In this section we briefly mention some implications for hard X-ray emission expected from our model, to place it into context with known results from hard X-ray observations of impulsive and microwave-rich events. Melrose & Brown (1976) considered an *effective number density* to illustrate the combined effect of having intensities from both thin and thick target sources. It is of the form

$$N_{\text{eff}}(\gamma, t) = N_{\text{trap}}(\gamma, t) + \frac{n_0}{n} \int_{\gamma}^{\infty} d\gamma' N(\gamma', t) \frac{v_p}{|\dot{\gamma}_c|}. \quad (9)$$

Here the first and second terms in the right-hand side represent the energy distribution of the high-energy electrons

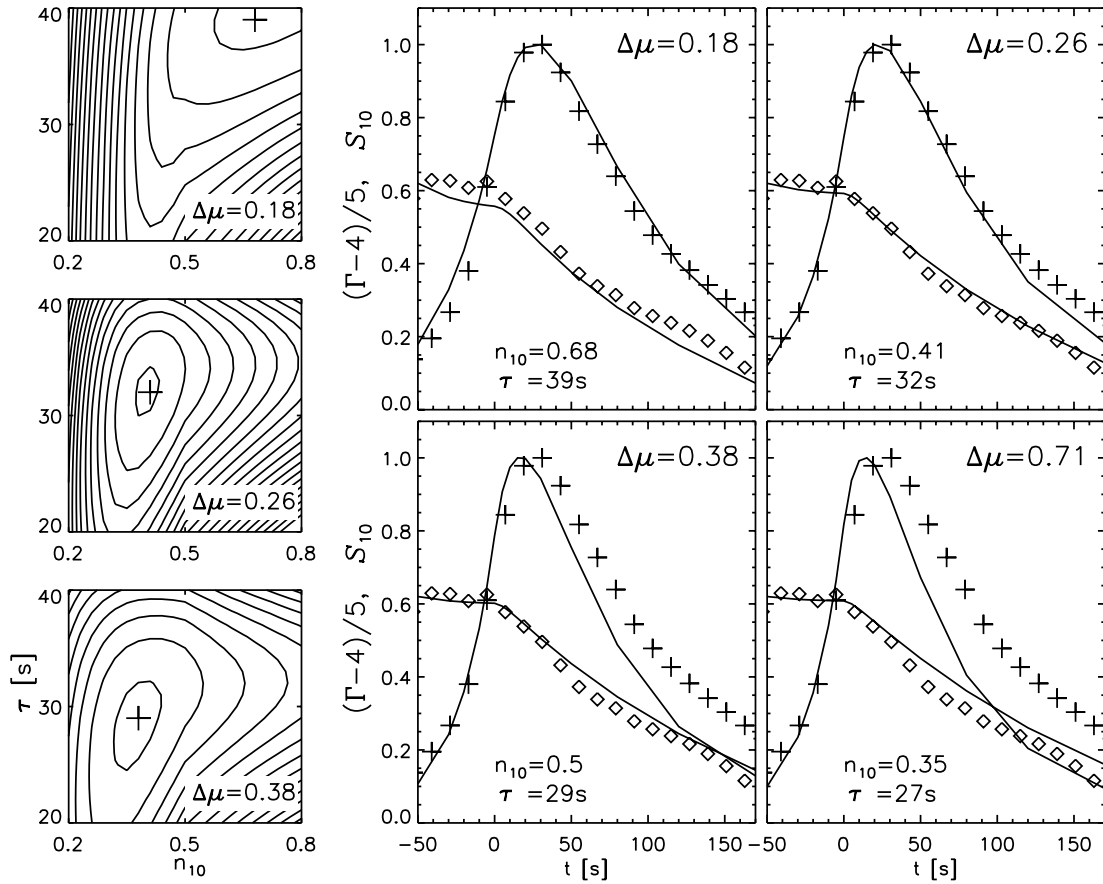


FIG. 9.—Model fit to the microwave observation under the hypothesis of beamed injection. *Left*: contours of goodness of model fit to the observation,  $\chi^2$  (see text for definition), where the contour levels are decreasing inward and the cross locates  $(n_{10}, \tau)$  giving the minimum  $\chi^2$  for each  $\Delta\mu$ . *Right*: Time profiles of the flux and spectral index at the corresponding parameter sets. Again crosses are the observed flux at 10 GHz and the diamonds are spectral index  $(\Gamma - 4)/5$ , and the lines are model fits. The best fit to the observation is found at  $n_{10} = 0.41$ ,  $\tau = 32$  s, and  $\Delta\mu = 0.26$ .

in the thin and thick targets, respectively, with  $N_{\text{trap}}(\gamma, t) = \int_0^{\mu_L} N(\gamma, \mu, t) d\mu$  and  $N(\gamma', t) = \int_0^1 N(\gamma', \mu, t) d\mu$ .  $n_0$  is the ambient density in the thick target and  $n$  is the density in the thin target, i.e., trap density.  $v_p$  is the rate of precipitation into the thick target and  $\dot{\gamma}_C$  is the rate of Coulomb energy loss in the thick target. There is an extra factor  $(n_0/n)$  in equation (9) compared with equation (28) of Melrose & Brown (1976) because we are regarding the thin and thick targets as physically separated. It is not necessary to know

the ambient density in the thick target,  $n_0$ , as it cancels out that in  $|\dot{\gamma}_C|$ .

An important parameter for this discussion is  $v_p$ , which plays the role of a second injection rate, into the thick target region, as compared with the injection rate into the thin target (coronal) region,  $q(t)$ . In the present model we can determine at each time step the proportion of electrons going into the loss cone (i.e.,  $\mu > \mu_L$ ). We therefore determine  $v_p$  from the time derivative of this quantity. Using the

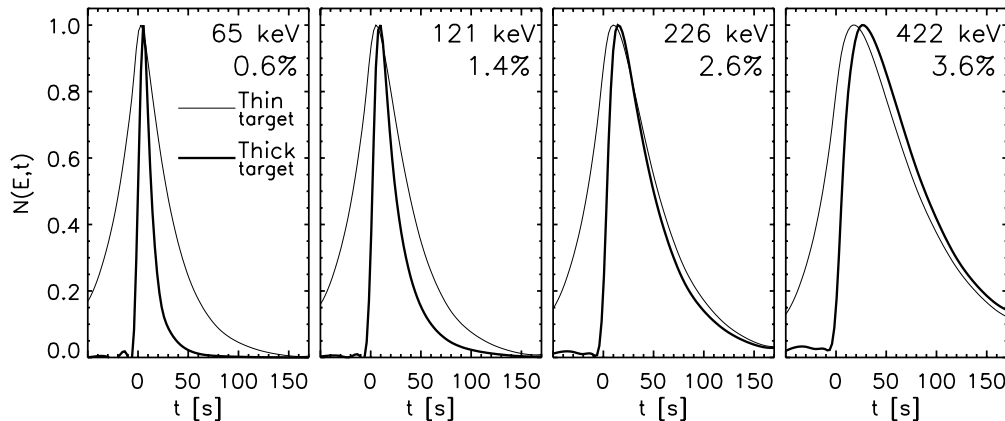


FIG. 10.—Relative time curves of the electron number density in the thin and thick targets. The numbers in the upper right corner in each panel denote the electron energy and the ratio of the maximum electron number density in the thick to thin targets, respectively.

best-fit model found in the previous section, we calculate the two quantities on the right-hand side of equation (9) as a function of time and show the results at four selected energies in Figure 10. Since we infer a very steep energy distribution, the photon emission rate at each energy is expected to vary in time similar to the  $N(E, t)$  curve at the corresponding energy shown in the figure. In terms of temporal behavior, the thin target emission resembles the injection function in the corona, whereas thick target emission is more impulsive and nearly symmetric around the peak especially at low energies. In all cases the thin target emission dominates by a large factor and the thick target emission is only a few percent of the thin target emission, a main reason for which is the low value of  $v_p$  lying in the range  $\sim 10^{-2}$ – $10^{-3}$  s $^{-1}$  as predicted by the present model.

Since thick target hard X-ray emission dominates in most flares, we should discuss why it is not the case in this particular event. If we confine ourselves solely to Coulomb collisions as a scattering and energy loss mechanism, thin target will dominate whenever the precipitation rate  $v_p$  is low, which requires a low density in the loop. As the density increases,  $v_p$  will increase, which increases the thick target emission, but thin target emission also increases proportionally. This discussion would indicate that thin target hard X-ray emission should dominate for all flares, so there must be another process operating in impulsive flares, in addition to Coulomb collisions, to enhance the precipitation rate. A good candidate is a process that enhances pitch-angle scattering to produce so-called strong diffusion (filling of the loss cone), which might be accomplished by an enhanced level of wave turbulence. The event presented in this paper, which we identified as a case of weak pitch-angle diffusion, cannot be such a case of high precipitation, and it is not a surprise that a thin target hard X-ray emission results.

## 7. CONCLUSION

We presented a case study of a microwave burst that occurred on 1993 June 3 observed using the OVSA, which is particularly interesting because its morphological and spectral behaviors appear to be consistent with the hypothesis of weak pitch-angle diffusion under Coulomb collisions, a physical process that is tractable by a straightforward theoretical modeling. A relatively simple model is developed for this purpose, in which we calculate the pitch-angle diffusion of trapped electrons with time in a specific magnetic field geometry derived from observations. We were able to fix the following parameters from observations as well: shape of the injection time profile (exponential) based on the observed flux in the rise phase, and the peak injection time from the turning point of the observed spectral index variation. Fixing all of these allows us to consider only three free parameters: the trap density,  $n_{10}$ , the injection time,  $\tau$ , and the injection beamwidth,  $\Delta\mu$ . We have assumed that the injection pitch-angle distribution is centered at the vertical incident angle,  $\mu_0 = 0$ . We find that the data are best fit by assuming an injection, with pitch angles confined to a

narrow range  $\Delta\mu(t = 0) \approx 0.26$  and a short injection time  $\approx 32$  s, into a magnetic loop with a relatively low density  $\approx 4.1 \times 10^9$  cm $^{-3}$ . This set of parameters identifies the burst as an event with good trapping, because of low density and beamed injection, rather than an event entirely driven by a time-dependent injection spectrum.

Previously, model results in favor of a narrow beamed injection have been presented by Leach & Petrosian (1981, 1983), McTiernan & Petrosian (1990), and Zharkova et al. (1995) in their studies of polarization of hard X-rays, which are emitted by electrons penetrating into the chromosphere. In comparison, our conclusion for a narrow beam injection is drawn from the spectral variations of microwave radiation from high-energy electrons trapped in the coronal part of the loop. The hypothesis of the isotropic pitch-angle distribution was rejected because with energy dependence of Coulomb collisions alone we could not reproduce the observation with any combination of free parameters. Two effects make microwave observations useful for diagnosing the injection pitch-angle distribution. One is that microwave radiation is strongly dependent on both the energy and pitch-angle distribution of high-energy electrons. The other is that microwaves arise from the trapped population, which can better preserve information about the injected electrons under Coulomb collisions. In terms of modeling techniques, those developed mainly to explain hard X-ray observations, such as the analytical model of Lu & Petrosian (1988) and the numerical models discussed by Zharkova et al. (1995), Fletcher & Martens (1998), and L. Fletcher & M. J. Aschwanden (2000, in preparation) are also applicable to this problem. However, the simplicity of the present model allows an efficient, systematic search for the best-fit model parameters that can be applied to specific microwave observations.

It is our next concern to extend the present study to a larger database of microwave bursts obtained with OVSA that show spectral hardening in the decay phase along with comparison with hard X-ray images. It appears that there are a significant number of such microwave bursts (Silva et al. 2000), although each event has to be checked to see whether it is due to Coulomb collisions and whether it is due to weak or strong diffusion, and the present model has to be extended accordingly. Once the characteristics of injections are known with better statistics it may help us to constrain the acceleration mechanism from such detailed properties. Physically, the narrow beam injection could be a consequence of a particular acceleration mechanism in combination with a specific magnetic field geometry. It will thus be important to compare results from these spectral analyses with magnetic topologies gleaned from observations in other wavelength regimes.

We thank T. Bai, T. Bastian, and M. J. Aschwanden for helpful comments. We also thank the anonymous referees for critical comments. The OVSA is supported by NSF grants ATM 97-96213 and AST 97-96238 and NASA grant NAG5-6381 to New Jersey Institute of Technology.

## REFERENCES

- Aschwanden, M. J. 1998, *ApJ*, 502, 455  
 Aschwanden, M. J., Bynum, R. M., Kosugi, T., Hudson, H. S., & Schwartz, R. A. 1997, *ApJ*, 487, 936  
 Aschwanden, M. J., Wills, M. J., Hudson, H. S., Kosugi, T., & Schwartz, R. A. 1996, *ApJ*, 468, 398  
 Bai, T. 1982, *ApJ*, 259, 341  
 Bai, T., & Ramaty, R. 1979, *ApJ*, 227, 1072  
 Bruggmann, G., Vilmer, N., Klein, K.-L., & Kane, S. R. 1994, *Sol. Phys.*, 149, 171  
 Dulk, G. A., & Marsh, K. A. 1982, *ApJ*, 259, 350  
 Fletcher, L. 1996, *A&A*, 310, 661  
 Fletcher, L., & Martens, P. C. H. 1998, *ApJ*, 505, 418

- Gary, D. E., & Tang, F. 1985, *ApJ*, 288, 385  
Gould, R. J. 1972, *Physica*, 60, 145  
Hamilton, R. J., Lu, E. D., & Petrosian, V. 1990, *ApJ*, 354, 726  
Kennel, C. F. 1969, *Rev. Geophys. Space Phys.*, 7, 379  
Klein, K.-L., Trotter, G., & Magun, A. 1986, *Sol. Phys.*, 104, 243  
Kundu, M. R., White, S. M., & Schmahl, E. J. 1989, *Sol. Phys.*, 121, 153  
Leach, J., & Petrosian, V. 1981, *ApJ*, 251, 781  
———. 1983, *ApJ*, 269, 715  
Lee, J., Gary, D. E., & Shibasaki, K. 2000, *ApJ*, 531, 1109  
Lu, E. T., & Petrosian, V. 1988, *ApJ*, 327, 405  
MacKinnon, A. L. 1986, *A&A*, 163, 239  
McTiernan, J., & Petrosian, V. 1990, *ApJ*, 359, 524  
Mel'nikov, V. F. 1994, *Radiophys. Quantum Electron.* 37, 557  
Mel'nikov, V. F., & Magun, A. 1998, *Sol. Phys.*, 178, 591  
Melrose, D. B., & Brown, J. C. 1976, *MNRAS*, 176, 15  
Melrose, D. B., & White, S. M. 1979, *Proc. Astron. Soc. Australia*, 3, 369  
Miller, J. A., & Ramaty, R. 1989, *ApJ*, 344, 973  
Nindos, A., White, S. M., Kundu, M. R., & Gary, D. E. 2000, *ApJ*, 533, 1053  
Petrosian, V. 1981, *ApJ*, 251, 727  
Petrosian, V., McTiernan, J. M., & Marschhauser, H. 1994, *ApJ*, 434, 747  
Ramaty, R. 1969, *ApJ*, 158, 753  
Silva, A. V. R., Wang, H., & Gary, D. E. 2000, *ApJ*, in press  
Takakura, T., & Kai, K. 1966, *PASJ*, 18, 57  
Vilmer, N., Kane, S. R., & Trotter, G. 1982, *A&A*, 108, 306  
Zharkova, V. V., Brown, J. C., & Syriavskii, D. V. 1995, *A&A*, 304, 284